A global-local damage localization and quantification approach in composite structures using ultrasonic guided waves and active infrared thermography

Kaleeswaran Balasubramaniam[1,*] ⓘ**, Shirsendu Sikdar**[2] ⓘ**, Dominika Ziaja**[3] ⓘ**, Michał Jurek**[3] ⓘ**, Rohan Soman**[1] ⓘ **and Paweł Malinowski**[1] ⓘ

[1] Institute of Fluid-Flow Machinery, Polish Academy of Sciences; Department of Mechanics of Intelligent Structures, Fiszera 14 Street, Gdansk 80-231, Poland
[2] Cardiff School of Engineering, Cardiff University, The Parade, Queen's Building, Cardiff CF24 3AA, United Kingdom
[3] Rzeszow University of Technology, Department of Structural Mechanics, Al Powstańców Warszawy 12, 35-959 Rzeszow, Poland

E-mail: kaleeswaranb@imp.gda.pl

CrossMark

Abstract

The paper emphasizes an effective quantification of hidden damage in composite structures using ultrasonic guided wave (GW) propagation-based structural health monitoring (SHM) and an artificial neural network (ANN) based active infrared thermography (IRT) analysis. In recent years, there has been increased interest in using a global-local approach for damage localization purposes. The global approach is mainly used in identifying the damage, while the local approach is quantifying. This paper presents a proof-of-study to use such a global-local approach in damage localization and quantification. The main novelties in this paper are the implementation of an improved SHM GW algorithm to localize the damages, a new pixel-based confusion matrix to quantify the size of the damage threshold, and a newly developed IRT-ANN algorithm to validate the damage quantification. From the SHM methodology, it is realized that only three sensors are sufficient to localize the damage, and an ANN- IRT imaging algorithm with only five hidden neurons in quantifying the damage. The robust SHM methods effectively identified, localized, and quantified the different damage dimensions against the non-destructive testing-IRT method in different composite structures.

Keywords: structural health monitoring (SHM), guided waves, composite structure, impact damage, non-destructive testing (NDT)

(Some figures may appear in colour only in the online journal)

---

* Author to whom any correspondence should be addressed.

1. Introduction

Composite materials are widely used in aerospace, automotive, construction, and several other engineering fields. Composite structures are preferred due to their lightweight and corrosion resistance [1] but, on the other hand, are prone to different damages. Impact damage occurs when a structure undergoes collisions/hits leading to cracks (with repeated collisions or hit with a high impact force) and finally a structural collapse. Barely visible impact damages (BVID) are one type of damage that is mostly not visible during the visual inspection and requires a touch-based inspection to examine further. They are mostly caused due to a tool drop/placing heavy loads leading to a small impact (dent) and are the initial cause of impact damage cracks [2]. The initiation of cracks starts on a micro-scale (not visible to the naked eye) wherein the inside matrix, layers break and when prolonged causes hairline cracks (HLC) [1]. Rapid identification of such damages is necessary as they reduce the strength of the structure and compromise structural integrity [3].

Damage detection methods need to be formulated to identify and quantify such small damages in composite structures. Various nondestructive testing (NDT) methods like terahertz spectroscopy [4], digital image correlation [5], laser Doppler vibrometer (LDV) [6], etc were proposed by researchers. However, the problem with these techniques is that the equipment employed for them is difficult to transport, heavy, and needs considerable time. Also, in most of the studies conducted the main focus was on identifying such damages and not on size/length/depth quantification-based parametric analysis.

The guided waves (GW) based damage detection approach using portable data acquisition transmitter and receiver (DAQR) with piezoelectric lead zirconate titanate (PZT) transducers is rapidly increasing in many engineering fields. They are lightweight, portable, and lesser time-consuming in gathering data [7]. These setups are used or in the testing phase by the industries for permanent, continuous online structural health monitoring (SHM) [1]. GW has the advantage of covering a larger surface area of the structure in a short interval of time. The understanding of transducer placements/optimization, signal processing methods, PZT types [1], dispersion curves [8], and material properties are essential in identifying the damages [9] with GW techniques. The use of only SHM-GW (global approach) in identification, localization, and quantifying smaller damages is examined further in this paper. The results are then supported by validating with the developed NDT- infrared thermography (IRT)- artificial neural network (ANN) scheme (local approach).

The damages studied in this research paper are BVID and HLCs of various lengths. BVID and HLCs are considered for the SHM-NDT study, as they are the initial causes of the strength reduction in the composite structures. Many researchers analyzed the SHM GW-based amplitude values drop changes at the impact regions in carbon fiber-reinforced polymer (CFRP) structures for damage identification [10–25]. *Boettcher et al* used GW to evaluate the impact of energy dissipation in structures [11]. CFRP structures subjected to

impact damages were analyzed using changes in wavelet energy and velocity variations by *Holst et al* [12]. A delamination study in an aluminum-carbon fiber structure using GW-based wavenumber mapping was performed by *Lugovtsova et al* [13]. GW scattering and reflection in CFRP structure with impact delamination [14] were analyzed by *Munian et al*. Using the time of arrival method, numerical damage models were compared against experimental results [15]. *Segers et al* used a GW-based nonlinear filtering technique in the damage localization of carbon fiber structures [16], and *Sha et al* analyzed damages in carbon composite structures using wavelet analysis [17].

Hervin et al studied GW scattering and entrapment at the impact damage crack zone [18]. *Dafydd et al* combined NDT and SHM techniques in the damage identification analysis of CFRP structure [19]. Multiple damages were localized using an ellipse-based approach [20] in a composite structure. *Azura et al* [21] utilized the reconstruction algorithm for probabilistic inspection of damage (RAPID) in the damage localization of CFRP structures. CFRP structures with damages were studied and localized using delay sum, signal differences, RAPID, and Voronoi-based algorithms [22, 23]. In most of the literature on SHM methods, damage localization was done using the entire actuator-sensor network. This increases the calculation time as it takes the entire coverage path of the sensors to validate the damage. The proposed SHM-GW methodology helps in damage localization with a reduced number of sensors with the help of a quick damage patch region identification methodology.

It was observed that most of the GW-based research works focus mainly on damage identification or localization [9, 10, 14–18, 22–24] and very few works deal with damage dimension estimation/quantification. The damage size measurements are key to industrial engineering as small surface impacts create HLC quickly in composite structures. A definite knowledge of damage size is required to come up with a decision on further using the structure or performing repairs. The quantification of impact damages and cracks is essential in estimating the structure's remaining life (prognosis- SHM level 4). Even though SHM analyses are promising, the current industrial world mainly uses NDT applications to verify structural integrity. So, the authors added a verification method using NDT-based IRT and also developed a new ANN imaging algorithm to quantify the verified damage. The main idea is to verify and compare the SHM results with the NDT method in damage quantification analysis. IRT was chosen among the several available NDT studies due to its quick visualization of the results. IRT has proven to be effective in material flaw identification analysis, crack identification, etc [25–27].

The literature shows that damage quantification studies on small cracks are rarely carried out. It was also observed that there are limited works on such damage localization with fewer sensors. The analysis with IRT generates huge data in the form of dynamic time step thermograms which need to be analyzed/classified quickly. An automated way of classifying and quantifying the damages using IRT was also not studied in detail in literature studies.

To overcome all the mentioned drawbacks, novelties using global-local SHM-NDT methodology are proposed in this paper to identify, localize, and quantify the mentioned damages. A mean absolute error (MAE)-based set method (global) is used to identify the damage paths and regions. To localize the damages (global) an improved wavelet transform coefficient (WTC) tomography-based approach is applied to the regions with few sensors. To quantify the damages (global) a new pixel-counting threshold-based confusion matrix analysis is applied to obtain the approximate dimensions of the damage. An effective NDT study using IRT-ANN is presented to cross-verify (local) the obtained parameterized results from SHM-GW and to classify the large data. The most significant benefit of the newly developed 'ANN-assisted IRT imaging' algorithm is the possibility of damage detection and automation. Thus, the damages (BVID, HLCs) are identified, localized, and quantified effectively using robust global-local-based techniques.

2. Methodology

The methodological overview of the global-local process is explained in the following steps;

- Study the dispersion characteristics of the specimen using a Dispersion calculator [28].
- Perform the SHM-GW analysis of the pristine specimens using DAQR.
- The next step is to perform an impact drop test on the pristine specimens converting them into a damaged state and then re-perform SHM-GW analysis using DAQR.
- Perform SHM-MAE study to identify damage paths (global—damage identification step) and MAE patch region study to approximate the area of damage. This is done using the intersection of sets (IOS) method as shown in figure 1 and explained further in section 4.2.1.
- Select the optimum frequency and localize the damage using SHM-GW techniques with the WTC tomography technique (global-damage localization step).
- Threshold-based quantification of the damages using a confusion matrix (global-damage quantification step).
- Implementing ANN-assisted IRT imaging algorithm to verify the damages (local-damage verification step).

3. Experimental analysis

3.1. Experimental samples

Case 1: A CFRP structure of dimensions $50 \times 50 \times 0.3$ cm^3 and made up of 12 layered prepreg $[0/90]_{3\,s}$ is taken as shown in figure 2. The composite structure has a BVID of Ø 1.1 cm and is made with an impact force of 25 J by dropping a steel ball (impactor) joined with a steel bar from a certain height guided via a pipe. The stiffener at the center is 0.4 cm thick and is rigidly attached to the structure. PZT discs are attached to the structure using cyanoacrylate glue, four on the left and four on the right side of the stiffener, based on sensor placement

optimization (elaborately described in [29, 30]) to monitor GW signals.

Case 2: figure 3 shows the CFRP structure of dimensions $20 \times 25 \times 0.5$ cm^3 and 16 layers arranged as $[0/90]_{4s}$. The structure has an HLC defect caused by an impact of 33 J (steel ball drop method which caused a deep dent on one side and protruded as HLC on the other). The length of the HLC initially made by the impact force is about 1 cm (subcase 1). Later, the crack is extended (1.5 cm—subcase 2 and 2 cm—subcase 3) with more impacts of the same energy. PZTs are attached in a linear rectangular format [31] to monitor the structure. The CFRP structures are procured from G.ANGELONI [32].

The material properties of the specimens obtained from the manufacturer are shown in table 1 and the global-local methods used in studying the CFRP samples are tabulated in table 2. IRT-NDT test was not performed for subcases 1, and 2 (table 2) as there is a high possibility of PZT detachment due to impact force and reattaching PZTs changes the entire experimental calculations. Thus, the NDT experiment was conducted after finishing the GW studies.

4. Global approach methodology, discussions, and results

4.1. Dispersion calculation results

The theoretical dispersion curves were calculated using Dispersion Calculator from Deutsches Zentrum für Luft-und Raumfahrt (DLR) and the obtained plots are shown in figure 4. The GW modes from the obtained signals are distinguished based on the standard velocity-distance relationship [1]. The dispersion curves were obtained by keeping an assumption of infinite plane wavefront and wave propagation in a direction normal to the wavefront [28]. The fiber orientations are symmetric and thus there are no or fewer changes in the dispersion curve plots for 0° and 90°. The A0 mode is selected as the GW mode for further research in this work because it is noted that it exhibits less variation at different angles (figures 4 and 5) and that, thanks to its shorter wavelength, it can detect even smaller defects [33]. The velocity values for the observed fundamental modes show very little variation up to a frequency of 250 kHz. Additionally, the amplifier used in the studies is only able to measure a maximum frequency of 250 kHz. As a result, a frequency limit of 200 kHz is selected for further testing.

As seen in figure 5, the group velocity values obtained from theoretical calculations are plotted in a polar plot (exemplary 150 kHz). The A0 mode is nearly constant in both cases, and S0 is stable at 0° and 90° but varies only at other angles. Similarly, SH mode is constant at 0° and 90° but varies at other angles.

4.2. SHM-GW studies using DAQR

DAQR setup is used to perform the GW analysis in cases 1 and 2. The experimental setup is shown in figure 6, which has a multi-transmitter and receiver connected to PZTs via a series
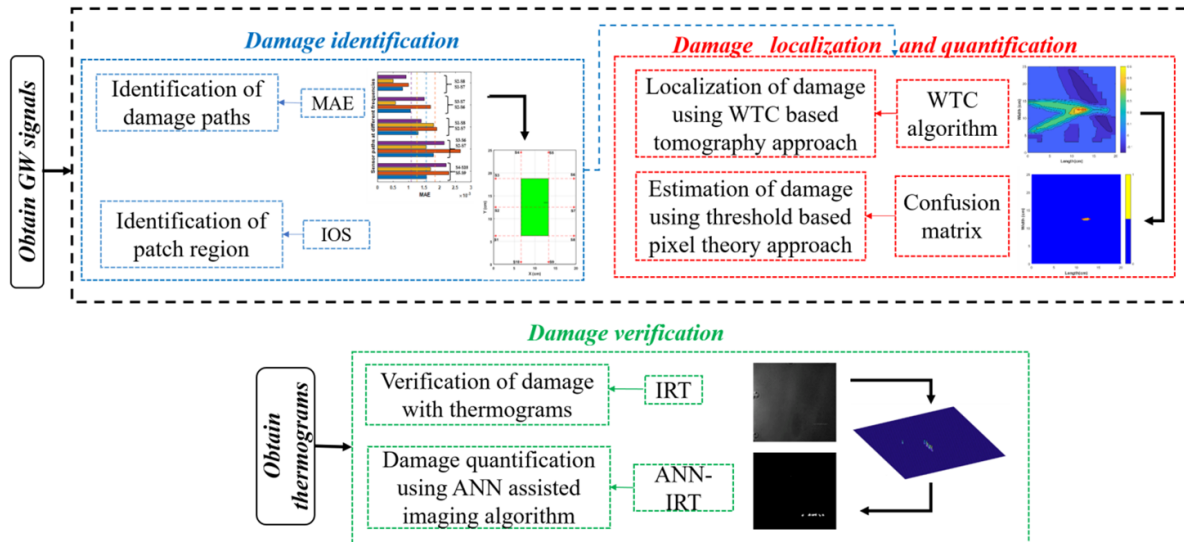
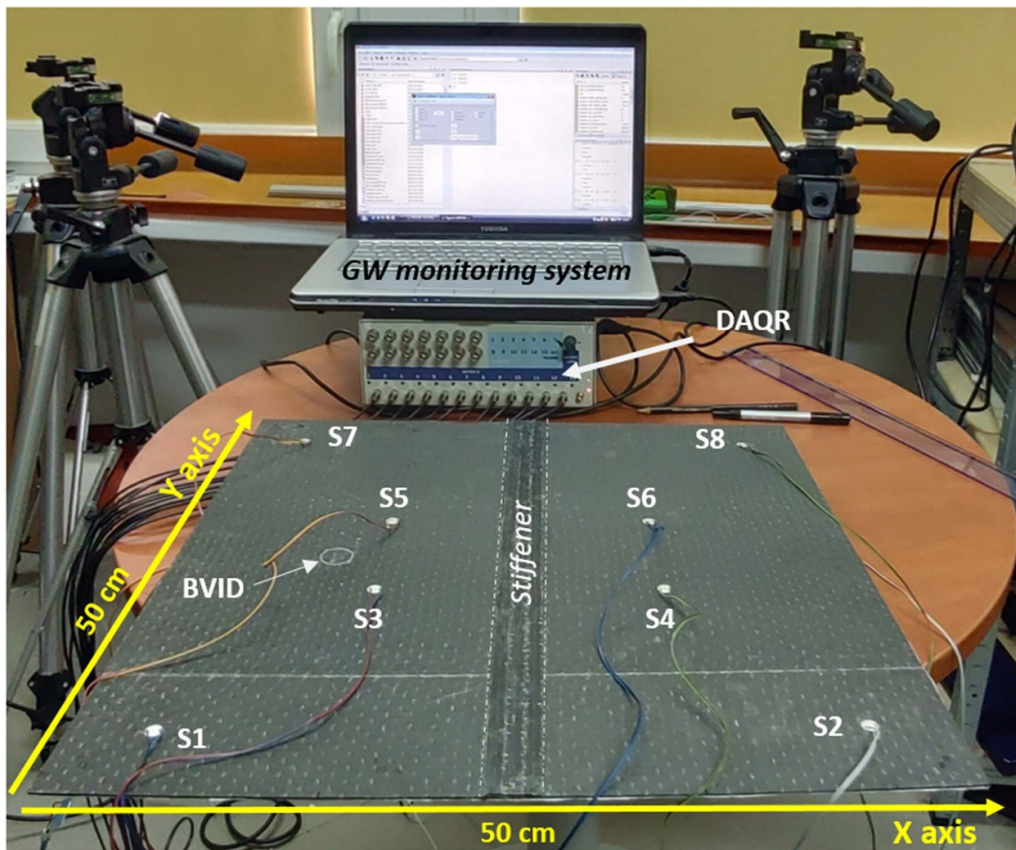**Figure 1.** Global-local assessment process.

Figure 2. Case 1: CFRP specimen with BVID [X axis = length, Y axis = width].

of wires. The setup has 13 channels in total, out of which 12 can serve as acquisition channels and one as receiving channel at one moment [24]. The setup is connected via a universal serial bus (USB) cable to the personal computer (PC). The excitation frequency, signal window, type, number of cycles, and channels are all controlled by a Matlab code. In this DAQR study, the PZT is used for excitation and sensing the GW. The PZT disc (Ø 1 cm) is made up of SONOX P502 material and is procured from CeramTec [34]. The CFRP structures are tested with GW excitation frequencies of 50, 100, 150, and 200 kHz, respectively. A 5-sine cycle Hanning windowed sine pulse is used for the GW excitation.
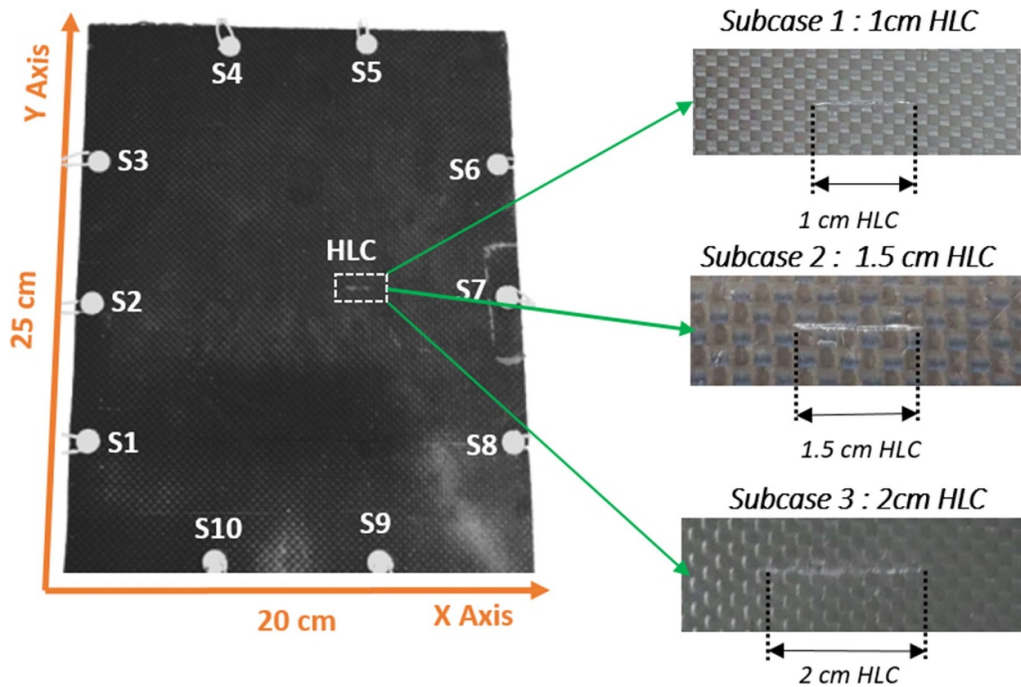
Figure 3. Case 2: CFRP specimen with HLCs of various lengths (subcases after impact).

Table 1. Material properties of the sample CFRP structures ['ρ' is the density, 'E' represents Young's moduli, 'G' is the shear moduli and 'Nu' is the Poisson's ratio].

Material	ρ (kg m^{-3})	$E_{11} = E_{22}$ (GPa)	E_{33} (GPa)	G_{12} (GPa)	$G_{13} = G_{23}$ (GPa)	Nu_{12}	$Nu_{13} = Nu_{23}$
CFRP	1568	75.89	10.0077	3.61	3.38	0.03	0.37
Adhesive	1150	4.052	4.052	1.447	1.447	0.40	0.40

Table 2. Damage cases, types, dimensions, and method of study.

Case	Damage type	Diameter/Length	Studied with
Case 1	BVID	1.1 cm diameter	GW-SHM and IRT-NDT
Case 2-Subcase 1	HLC	1 cm length	GW-SHM
Case 2-Subcase 2	HLC	1.5 cm length	GW-SHM
Case 2-Subcase 3	HLC	2 cm length	GW-SHM and IRT-NDT

4.2.1. MAE analysis using DAQR signals. The GW signals obtained from DAQR are tested with MAE [1, 7] as shown in equation (1) to identify the healthy and damage paths. Sensor pair paths studied using MAE are shown in table 3. If any signal paths show higher MAE, then a line is drawn to connect the signal paths (based on the exemplary IOS-figure 7) thereby creating an area (patch). The method acts as a referential free and helps to capture the region where higher MAE values are obtained thereby assuming it as the region of damage (patch). MAE is an effective damage index method and is used on similar nonhomogeneous structures [35].

$$\text{MAE (i,j)} = \frac{1}{n} \sum_{t=1}^{n} |(S_i - S_j)| \qquad (1)$$

where: 't' is the time starting from 1 till n, and S_i and S_j are the magnitude values of the signals.

4.2.2. Damage identification using MAE results. In the MAE (equation 1 signal path analysis, it is found that specific signal pair paths show higher MAE values. Such variation in the MAE is due to variation of signal amplitude that occurred due to damages when the signal paths are crossing the damage or near the damage. An exemplary S5S3 and S6S4 signal of 100 kHz (figure 8(a)) shows the incident and reflection due to damage, and figure 8(b) with S5S9 and S4S10 signals also show a similar trend of reflection due to damage. This proves the reason for higher MAE values from such signal paths.

The signal paths S4S6 and S3S5 in case 1 (figure 9(a)) and S4S10 and S5S9 (case 2- figure 9(b)) show a higher MAE values variation, confirming the disturbance in the signals due to damage. Threshold values are made based on the mean value (MV) of each frequency, and the signal path that crosses the threshold limits is chosen as the damage path. In most cases, 150 kHz gave maximum MAE values and thus was selected as a targeted/optimal frequency for WTC analysis. Similar MAE step process results are obtained for cases 2: subcases 2 and 3, respectively.

The IOS patch (figure 10) is created (yellow region) by connecting the signal paths with a high value of MAE signals from cases 1 and 2. The patch identifies the particular region where
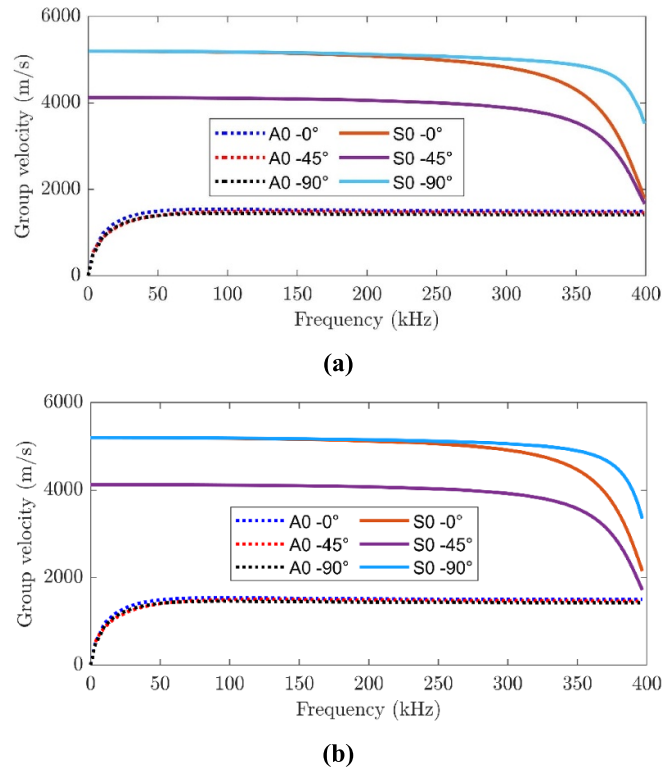
(a)

(b)

Figure 4. Theoretical dispersion curves: (a) case 1, (b) case 2.

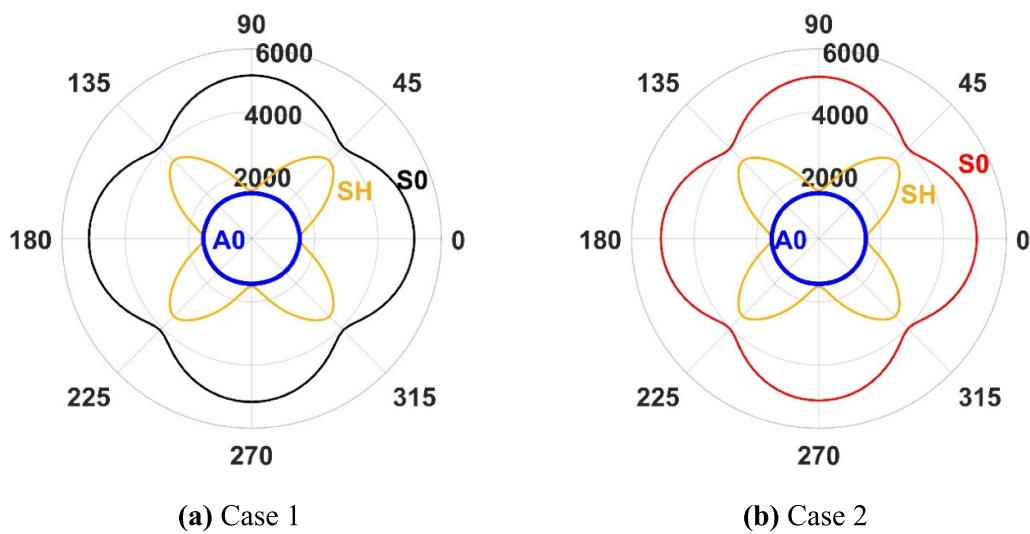**(a)** Case 1　　　　　　　　　　　　　　**(b)** Case 2

Figure 5. Polar plots showing group velocity (m/s) at various angles in degrees ($^{\text{o}}$).

further analyses needed to be studied using specific sensors, thereby eliminating the calculation time for SHM-WTC and human labor time for NDT-IRT analysis.

4.2.3. WTC analysis using DAQR signals. The implemented SHM algorithm uses the WTC of the registered GW signals (in the time domain) from the PZT networks assigned to cases 1 and 2. The algorithm uses input GW signals obtained from the sensors identified using the MAE patch region.

The localization algorithm calculates the differences in WTC magnitudes at each PZT-to-PZT path in cases 1 and 2. The experimental DAQR A0 mode velocity values, which are used in the WTC algorithm, have good agreement with theoretical calculations. The algorithm [36] is improved to study the identified patch regions with a limited number of sensors and for centimeter range damages. The BVID index (B_I) is calculated based on the root-mean-square change in WTC magnitudes of the GW signals from the selected sensor pairs, as shown in equation (2).
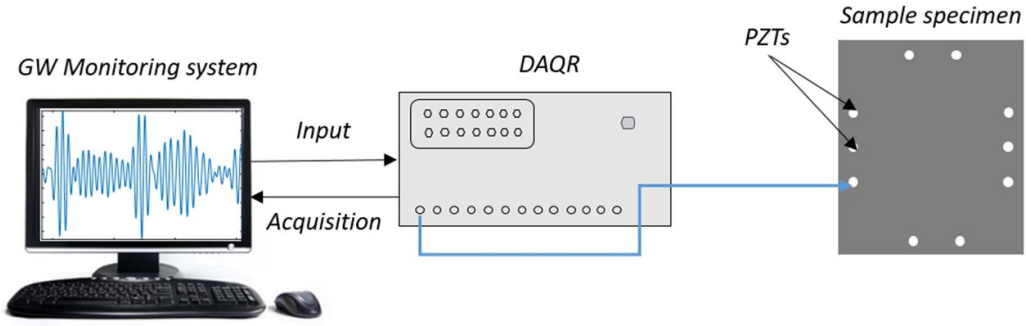
Figure 6. Schematic DAQR setup for an exemplary Case 2.

Table 3. Case 1, case 2: signal paths studied for 50 100 150, and 200 kHz.

Case 1		Case 2	
S_i	S_j	S_i	S_j
S2S4	S1S3	S4S10	S5S9
S4S6	S3S5	S3S6	S2S7
S6S8	S5S7	S1S8	S2S7
S1S7	S2S8	S3S7	S2S6
		S2S8	S1S7
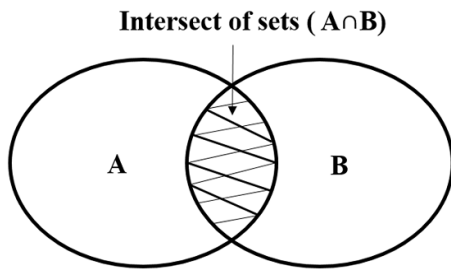
Figure 7. Intersect of set calculation (example).

$$B_{I_{ij}} = \sqrt{\frac{\left\{\int_{t_1}^{t_2}(\text{WTC}_i + \text{WTC}_j)^2 dt\right\}}{\left\{\int_{t_i}^{t_2}(\text{WTC}_i)^2 dt\right\}}} \quad (2)$$

where: 't_1' and 't_2' are the selected limits of the transformed input signals in the time domain, and 'WTC$_i$' and 'WTC$_j$' are the amplitude areas of the WTC of any sensor pair: PZT#i, PZT#j.

The BVID-source probability indicator, 'B_I' for any position (x, y) within the PZT network can be represented as a linear summation of the obtained $B_{I_{ij}}$ (equation (3) from every possible PZT pair, each of which has a spatial distribution as in equation (4).
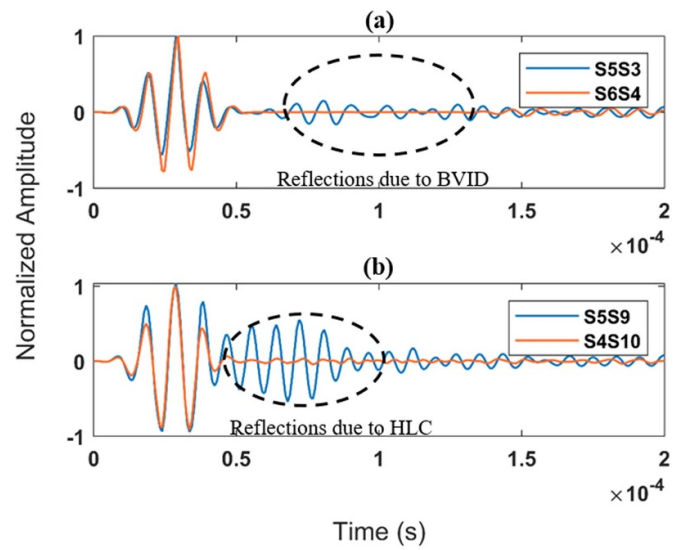

Figure 8. Comparison (a) case 1 signals, (b) case 2- subcase 1 signals.

$$B_I(x,y) = \sum_{i=1}^{n-1}\sum_{j=i+1}^{n} B_{I_{ij}}\alpha_{ij} \quad (3)$$

Where: 'α_{ij}' is a non-negative and linearly-decreasing spatial distribution function expressed as:

$$\alpha_{ij} = [\{\phi - L_{ij}(x,y)\} / (\phi - 1)] \quad (4)$$

In equation (4), the scaling parameter controls the size of the effective elliptical distribution area of each sensor-sensor pair. In the spatial distribution function, $L_{ij}(x,y)$ it is expressed as-

$$\begin{aligned} L_{ij}(x,y) &= p_{ij}(x,y), \text{ for } p_{ij}(x,y) < \phi \\ L_{ij}(x,y) &= \phi, \text{ for } p_{ij}(x,y) \geq \phi \end{aligned} \quad (5)$$

Where:

$$p_{ij}(x,y) = \left[\left\{\left(\sqrt{(x-x_i)^2 + (y-y_i)^2}\right) + \left(\sqrt{(x-x_j)^2 + (y-y_j)^2}\right)\right\} / s_{ij}\right] \quad (6)$$
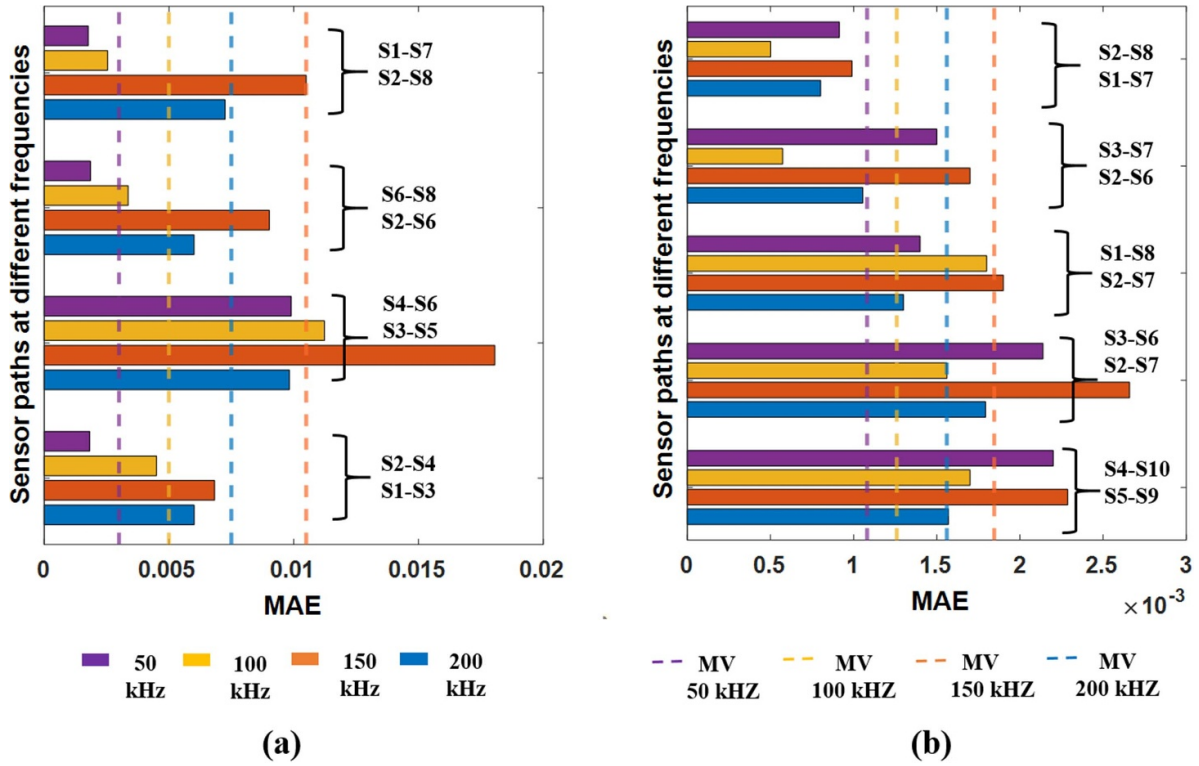
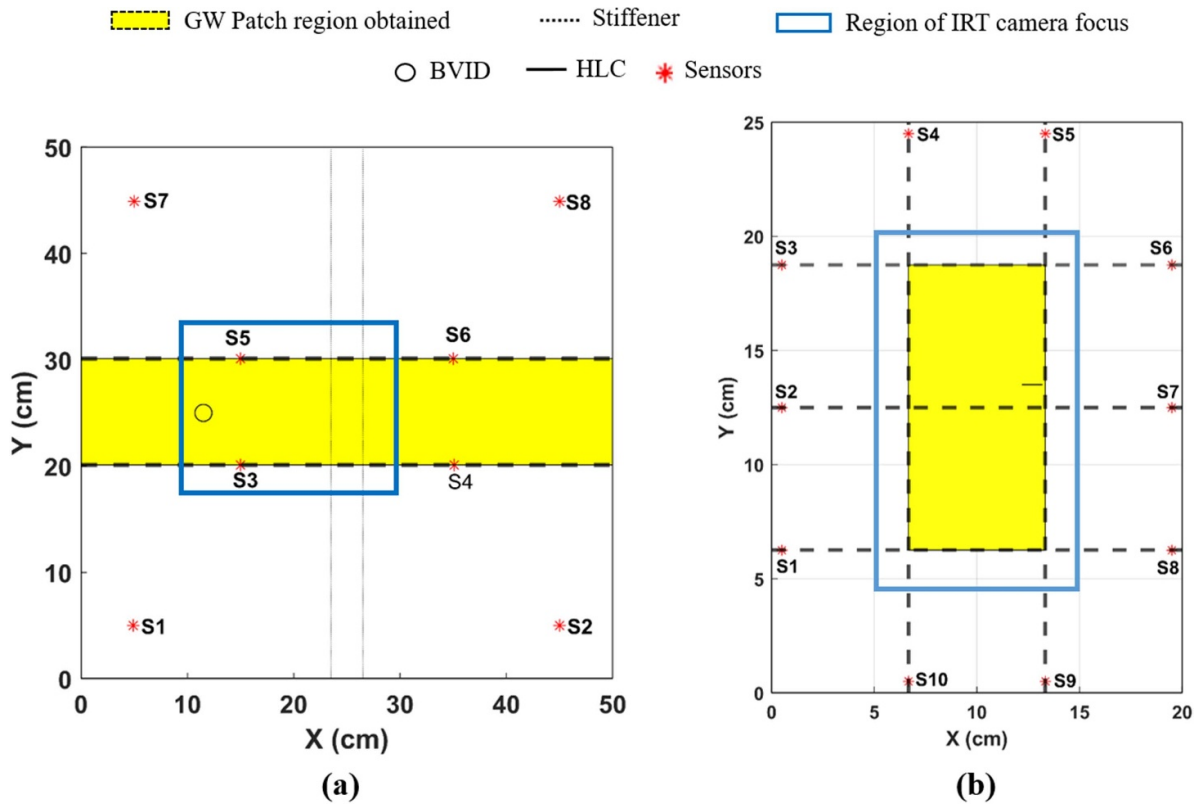**Figure 9.** MAE results for 50–200 kHz excitation: (a) case 1, (b) case 2—subcase 1.

Figure 10. Patch region obtained based on the IOS (a) case 1, (b) case 2.

(a) Case 1

(b) Case 1 threshold

(c) Case 2 (subcase 1)

(d) Case 2 (subcase 1) threshold

(e) Case 2 (subcase 2)

(f) Case 2 (subcase 2) threshold

(g) Case 2 (subcase 3)
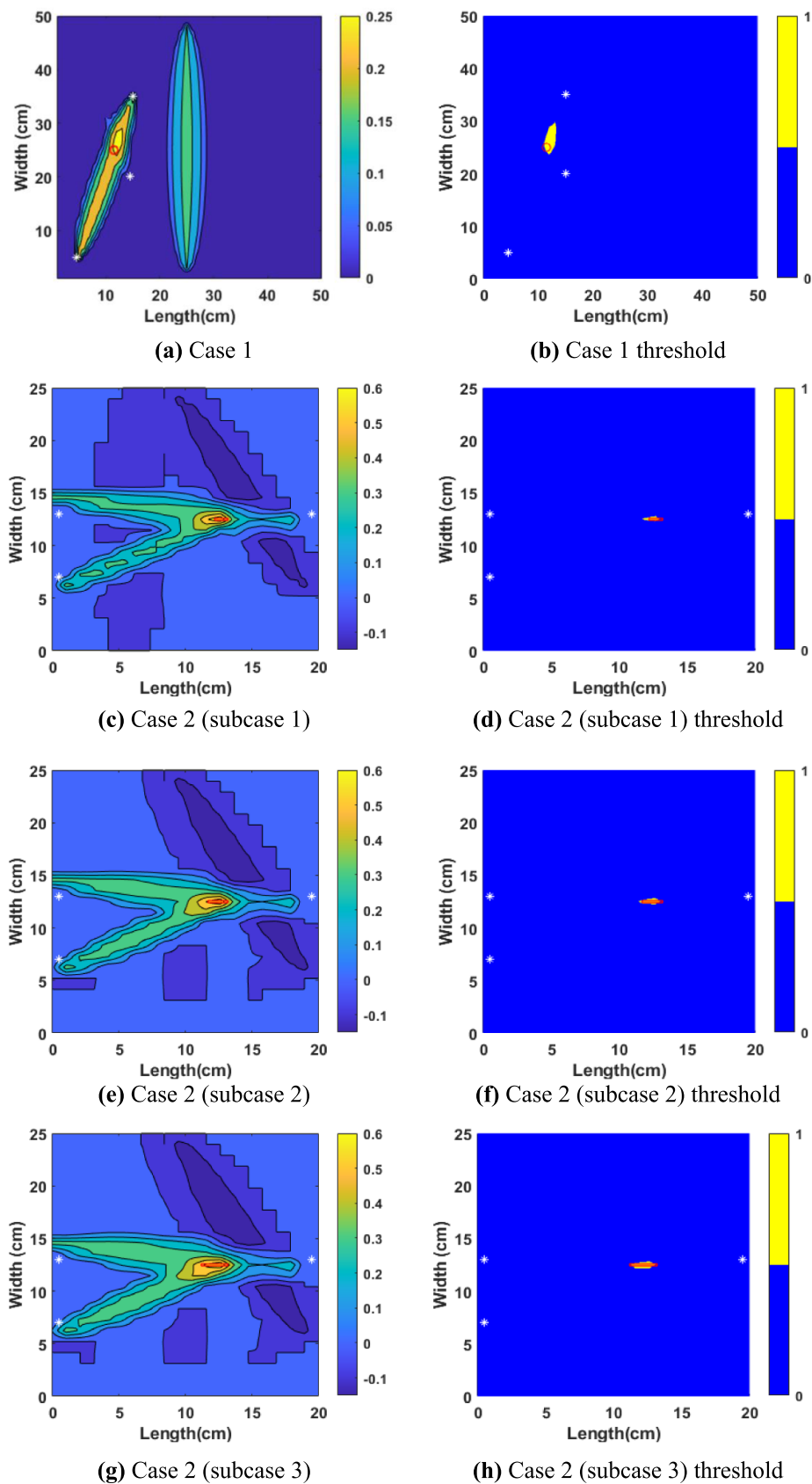
(h) Case 2 (subcase 3) threshold

Figure 11. Damage-index maps: (a) case 1 contour map, (c, e, g) case 2 contour maps, (b) case 1 threshold map, (d), (f) and (h) case 2 threshold maps.

'S$_{ij}$' is the sensor-sensor distance, and 'ϕ' is a scaling parameter (empirically assumed to be 1.03 and tested for anisotropic materials) that controls the size of the elliptical distribution area of each sensing path. Artifacts will be introduced if ϕ is too small, and resolution is lost if ϕ is too large. Generally, if a defect occurs, a set of sensor pair signals will be affected. As a result, in the defect distribution probability image, the point where the defect is located will have a dominantly larger probability compared to the other points. Consequently, by applying image processing techniques, such as judiciously selecting a threshold (ϕ) to the defect estimation image, the defect location can be estimated.

The SHM strategy is implemented in MATLAB that calculates an (8 × 8) matrix with 64 combination signals as inputs from the assigned sensor network of 8 PZTs. In the process, the combinations of sensor paths: S#1-1, ..,,1–8; S#2-1, .., 2–8; 3–1; S#3-1, .., 3–8; S#4-1, .., 4–8; S#5-1, .., 5–8; S#6-1, .., 6–8; S#7-1, .., 7–8; S#8-1, .., 8–8; (refer to Case 1: figure 2(a)) are considered to image the predicted BVID regions. A similar strategy is also applied to case 2: figure 2(b) which has 10 PZTs respectively.

The WTC algorithm was found to be effective in localizing and even quantifying the damage (BVID, HLCs) in the investigated composite structures. In past, the online monitoring of CFRP structures using continuous wavelet transformation [12] identified only the presence of damage. Damage quantification using local wavenumber mapping [13] did show the size of the damage, but the method uses LDV which requires full-area scanning. Similarly, the size of the damages was analyzed using 2D wavelets [17] and using GW scattering [18] which were based on LDV measurements. SHM GW analysis to predict the location of the BVID was shown in [19] using an ellipse-based localization algorithm. The method possibly may fail to detect if the damage is close to the actuator. Results using the RAPID algorithm [21] and Delay Sum algorithm [22, 23] helped the researchers to localize the presence of damages in CFRP structures but were not used for the quantification.

4.2.4. Damage localization using WTC results. The BVID localization WTC maps generated for case 1 are presented in figure 11(a), and similarly, HLC regions of case 2 subcase 1 in figures 11(c) and (e) subcase 2, and figure 11(g) subcase 3 respectively. The cases shown in figure 11 correspond to the cases in table 2, respectively. For case 1, sensors S1, S3, and S5 are chosen for localization based on MAE patch results. Similarly, for case 2, only 3 sensors S1, S2, and S7, are selected. In case 1 (figure 9(a)) for example the highest MAE is found for the S3S5 pair and the next highest is for the S1S7 pair. The signals obtained for the S1S3 pair showed higher amplitude variations than S5S7. So, based on this S1, S3 and S5 were found to be the tradeoff choice for choosing the triangulation sensors for WTC-based damage localization. The selection of sensors is based on paths that showed higher MAE values. The contour plots identified the damages based on higher values

Table 4. Calculation time for damage localization using the WTC algorithm.

Case	Localization time with all sensors (s)	Localization time with few sensors after the MAE process (s)
1-BVID	115	87
2- Subcase 1 HLC	147	34
2- Subcase 2 HLC	145	43
2- Subcase 3 HLC	139	54

of WTC magnitudes. Threshold pixel plots (figures 11(b), (d), (f) and (h)) of the 85% threshold region (shown in the yellow color of binary value = 1) helped to show the approximated damage size and lengths against the original damage size (red color circle, rectangle).

It can be seen from the results of threshold maps that the shape of the damage is captured well (except in case 1) for the chosen optimal threshold value. The results obtained proved that such a low number of sensors are sufficient for damage localization. The entire calculation was performed on an Intel i5 processor 32GB RAM workstation. The calculation time of the process is shown in table 4 with and without the MAE process.

4.2.5. Damage quantification using the confusion matrix. The optimal value for the damage quantification threshold (85%) was selected using the pixel counting-based confusion matrix metrics as shown in figures 12 and 13, and equation (7). Some researchers mainly used confusion matrix accuracy formulations in damage classification [37]. A confusion matrix-based scheme is used in damage quantification in this research work. The threshold percentage value tends to change based on different structures and thus a quick run with the developed confusion matrix scheme helps to identify the best quantification percentage value for the calculation.

The confusion matrix is a popular way of seeing the performance of the predicted values against the original values. The confusion matrix consists of two classes, i.e. positive and negative. The confusion matrix helps us understand the predicted model in a simple and better way. In this paper, confusion matrix-based metrics are used to determine which percentage (threshold) the damage detection is better, thereby showing the size and length of the detected damage cases.

The total number of mesh grid points (pixels) in each of the case studies (table 5) is denoted by 'M', and the number of pixels representing the original damage size is referred to as 'DP' (marked with a red color circle or rectangle in figures 11 and 13), and the number of pixels predicted after applying threshold condition is 'P' (marked with yellow color pixels-figure 13). It is also called growth truth or positive.

$$N = M - P; \; TP = DP - FN; \; FP = P - TP; \; TN = N - FN$$
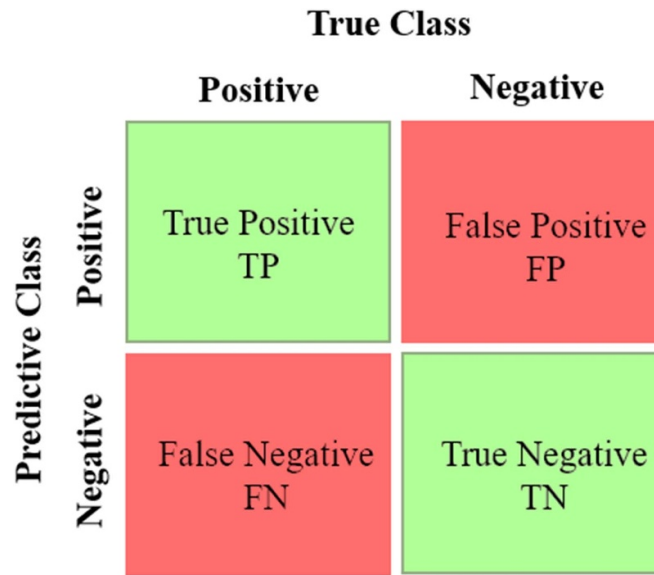$$(7)$$

True Class

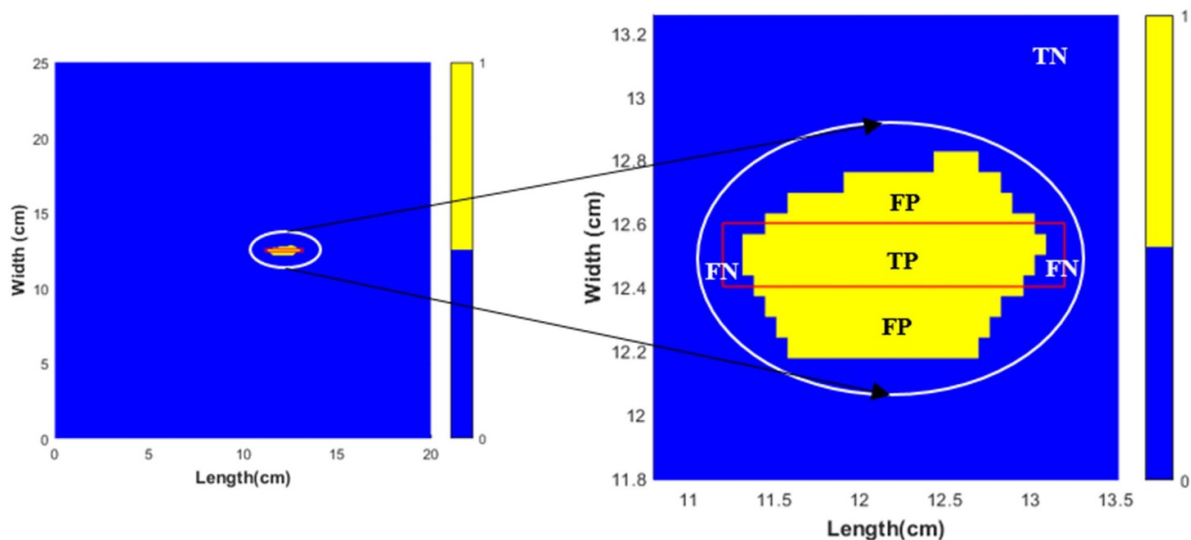**Figure 12.** Pixel counting-based confusion matrix.

Figure 13. Damage quantification is based on pixel counting (e.g. case 2- subcase 3).

where: *N* is the total negative pixels present in the case study specimen, TP refers to the number of pixels that are within the DP excluding the FN, FN is the number of falsely predicted pixels within the DP, FP is the number of false pixels that are present outside the DP but within the calculated predicted growth truth P, TN is the total number of negative pixels (*N*) that are present in the whole case study specimen neglecting the FN. These terms are then used to calculate the other confusion matrix terms as shown in equation (8) and (9).

$$\text{Percentage Index } (\text{PI})\% = \left(\frac{\text{TP}}{\text{DP}}\right) \times 100 \qquad (8)$$

Miss hits $(\text{MH}) = \text{FP} + \text{FN}$; Miss hit percentage $(\text{MHP})\%$

$$= \left(\frac{\text{FN}}{\text{P}}\right) \times 100 \qquad (9)$$

Where: PI denotes the percentage of TP in DP, sensitivity refers to the proportion of positive cases predicted, MH refers to the total number of miss-hits (positive and negative) present within *N*, and MHP is the FN percentage in *P*.

The threshold determination is shown in figure 14 for all the cases with 75% –100% (in 5% steps) limits and based on the threshold limits, the confusion metric factors are determined. The damage detection criteria kept are that mishits (MH)

Table 5. Constant values used in the confusion matrix calculation [pixel numbers = px].

S.No	Cases	M (px)	DP shape	DP (px)
1	Case 1	250 001	Circle	177
2	Case 2-Subcase 1	117 425	Rectangle	64
3	Case 2-Subcase 2	117 425	Rectangle	88
4	Case 2-Subcase 3	117 425	Rectangle	120

pixels should be as low as possible, and the PI index should be higher to indicate detected damage. In figure 14(a), the overall mishits are mostly the same for cases 2, 3, and 4 and reduce drastically for case 1 after the 90% threshold, but the PI percentage is lower (figure 14(b)). This shows that the size of the damage is not clearly and correctly identified. Also, it can be seen in figure 14(c) that the MHP values increase significantly after 85%.

To arrive at a tradeoff value, the normalized values of FP and FN are plotted against each other (figure 14(d)). An intermediate region is obtained where both the curves meet, and it lies mainly at 85%. It should be mentioned that 85% also identify the approximate shape of all the mentioned damages in a very desirable way. To put together, all the results obtained (figures 11(b), (d), (f) and (h)) are tabulated in table 6, wherein the pixel dimensions are 0.1 mm (for both *x* and *y* axes) for case 1, and for case 2 is 0.05 mm (*x*-axis) and 0.08 mm (*y*-axis) respectively for all the three subcases of case 2. The calculation of the area/diameter of the damage for case 1 is neglected as the damage is not bound within the DP.

5. Local approach methodology, discussions, and results

5.1. NDT studies using IRT-ANN

An active IRT experimental analysis of the composite structures is performed using FLIR SC6540 [38]. It measures the temperature distribution and identifies patterns in the thermograms for visualizing the presence of defects. The heat source is the halogen lamp with a maximum power of 1.3 kW. The halogen lamp (heat source) and IRT camera are then focused only on the MAE patch region (figure 10 to perform the IRT analysis. The CFRP specimens are heated for 10 s, and the cooling process is registered for 15 s. Recorded sequences of thermal images (thermograms) are processed with Automation Technology GmbH IrNDT software [39]. A schematic setup schema of impulse thermography is shown in figure 15.

During the laboratory measurements, the ambient temperature was constant and stable. The surface of the test sample was not exposed to sunlight, nor to flowing warm or cold air. The influence of the initial temperature of the tested object, being a consequence of the ambient temperature, was taken into account at the stage of processing the recorded thermograms. The sequence of maps, which were subjected to further processing, was obtained as the difference between the thermograms recorded in the subsequent moments and the first thermogram recorded at the beginning of the measurement.

In the performed analysis, functions approximating the signal recorded in each pixel of the analyzed area are determined.

It made it possible to generate maps of any parameters of the designated functions. In further analysis, maps of the value of the second derivative at a selected time instant are used. The choice of such a parameter resulted from the preliminary analysis of the recorded thermal responses. It is found that the second derivative of the functions approximating the recorded signals contains more information allowing to locate the damaged site. The radiation of the sample is analyzed with digital level as the unit to simplify the process [40].

5.1.1. ANN-IRT-based image reconstruction algorithm. The main concept of the proposed ANN-IRT-based damage detection is shown in figure 16.

ANN studies [41] mostly deal with GW-based numerical measurements as it is possible to obtain data in large numbers/large quantities [35, 42]. ANN is not the typical tool used for the analysis of data obtained with IRT methods. However, their ability for generalization and important feature extraction makes them suitable for the investigation of huge databases collected during IRT examinations. There are two ways for IRT thermal effect analysis-it is possible to analyze the separate step registered by the IR camera (presented in [43]) or the whole heating/cooling process (what is presented here). The heating/cooling process can be approximated by the functions specified for each point of the observed specimen.

In figure 17, the examples of maps for different parameters obtained for the sequence of thermograms are presented. The pictures in figures 17(a)–(f) are connected to the same specimen, the same measuring configuration, and the same point of time (12th frame of the cooling process). The selection of the right frame is determined by expert experience in the stage of tool preparation. Different parameters are calculated based on the same data for the whole cooling process. As can be seen, obtaining massive databases is relatively simple, but analyzing them is more troublesome and time-consuming when more parameters are considered. The operator's experience is crucial.

The algorithm, shown in figure 16 can be mathematically described as follows. For each pixel registered by the IR camera, the heating/cooling process approximating function $g_{i,j}(t)$ is established. The location of the pixel (measurement points) is described on the surface by the number of its row (*i*) and column (*j*). Then the *n*th derivative of the above-mentioned function is calculated (equation (1)).

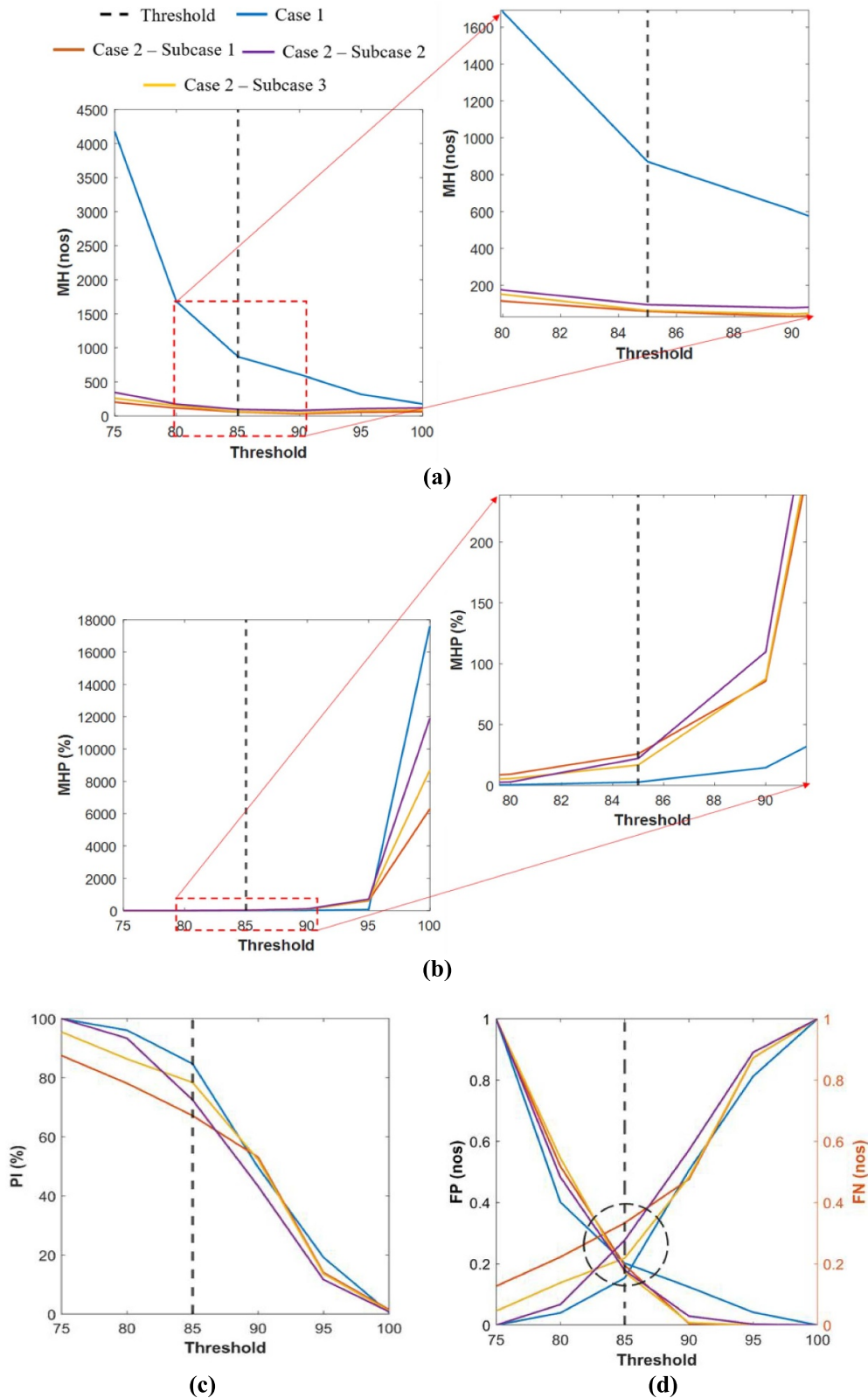$$dg_{i,j} = \frac{d^n g_{i,j}(t)}{dt^n} \qquad (10)$$

Figure 14. (a) Threshold (vs): (a) MH, (b) MHP, (c) PI, (d) FN, FP.

where: t-time of observation, *n*-the optimal order of the derivative, selected arbitrarily based on previous experience considering the examined material and measurement configuration, here *n = 2*.

Next, the time step and color scale are selected as shown in equation (11):

$$dg\,(i,j) = s\,(dg_{i,j}\,(t_0)) \qquad (11)$$

Table 6. Damage dimensions obtained using a confusion matrix [ADP = Approximated damage pixels, ADD = Actual Damage Dimensions, add = approximate damage dimensions, Absolute Difference = AD].

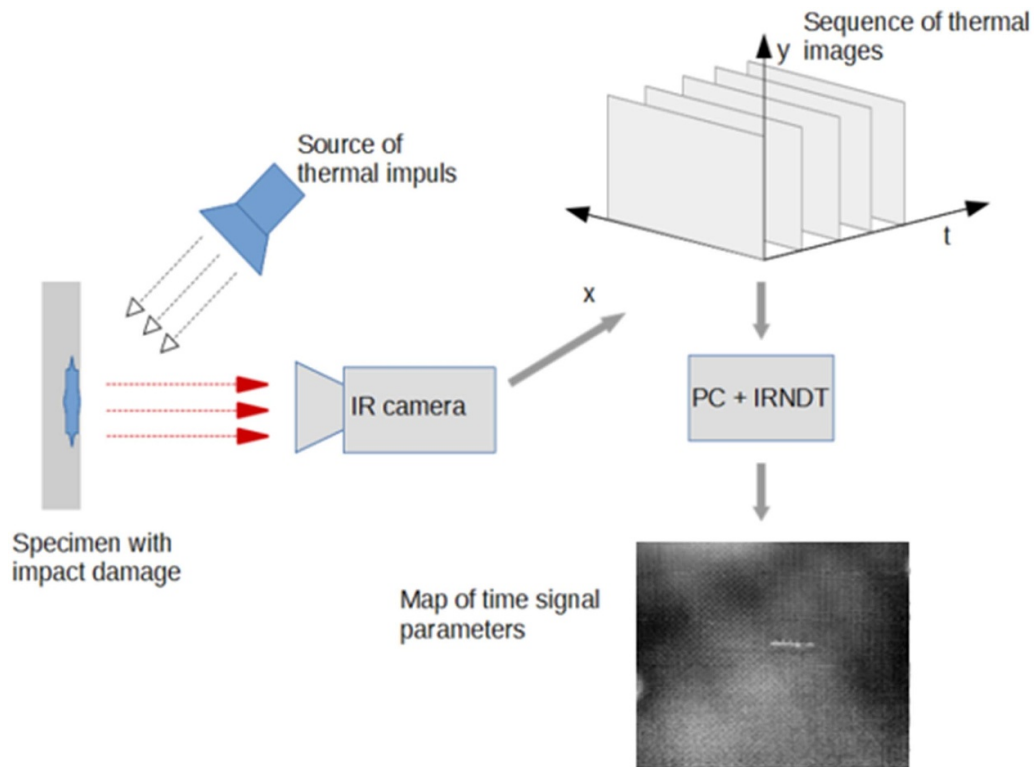| Case	DP (px)	ADP (px)	ADD (cm)	Add (cm)	AD |ADD-add| (cm)
1	177	504	Ø 1.1	1.8 × 4.9	–
2 -Subcase 1	64	81	1 × 0.1	1.2 × 0.11	0.2 × 0.01
2-Subcase 2	88	113	1.5 × 0.1	1.4 × 0.14	0.1 × 0.04
2 -Subcase 3	120	149	2 × 0.1	1.7 × 0.26	0.3 × 0.16

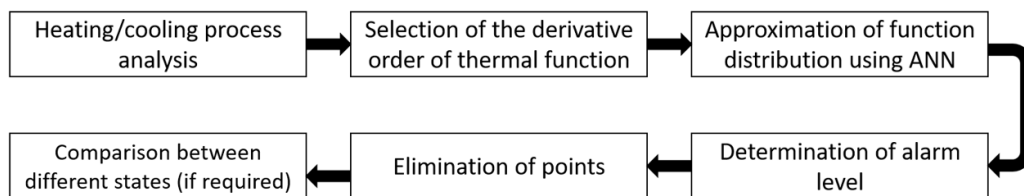**Figure 15.** IRT schema of impulse thermography analysis.

Figure 16. The main concept of the presented new ANN-IRT algorithm.

Where: s is the color scale function, here the greyscale is adopted, so $dg(i,j) \in \langle 0, 255\rangle$, t_0 time step in the heating/cooling process selected arbitrarily by the operator; once established t_0, as well as s are constant for all measuring points.

The distribution of the $dg(i,j)$ function above the specimen surface is made using artificial neural networks (equation (1)).

$$f_{ANN}(i,j) = ANN(\{i,j\}, w) \qquad (12)$$

where: ANN is a satisfactorily trained artificial neural network with the network parameters collected in w vector. This vector is established during the minimization of mean square normalized error (MSE) between the network output and target value

for points selected in the learning data set. The learning set of data consisted of patterns $P_k = \{\{i_k, j_k\}, dg(i_k, j_k)\}$, where k is the number of patterns. In the analyzed task to learning, data set the measuring points on the crossing of every 20th row and 20th column are selected. Finally, for each measuring point the $f(i,j)$ function is calculated as follows:

$$f(i,j) = dg(i,j) - f_{ANN}(i,j) \qquad (13)$$

and then the Alarm level (AL):

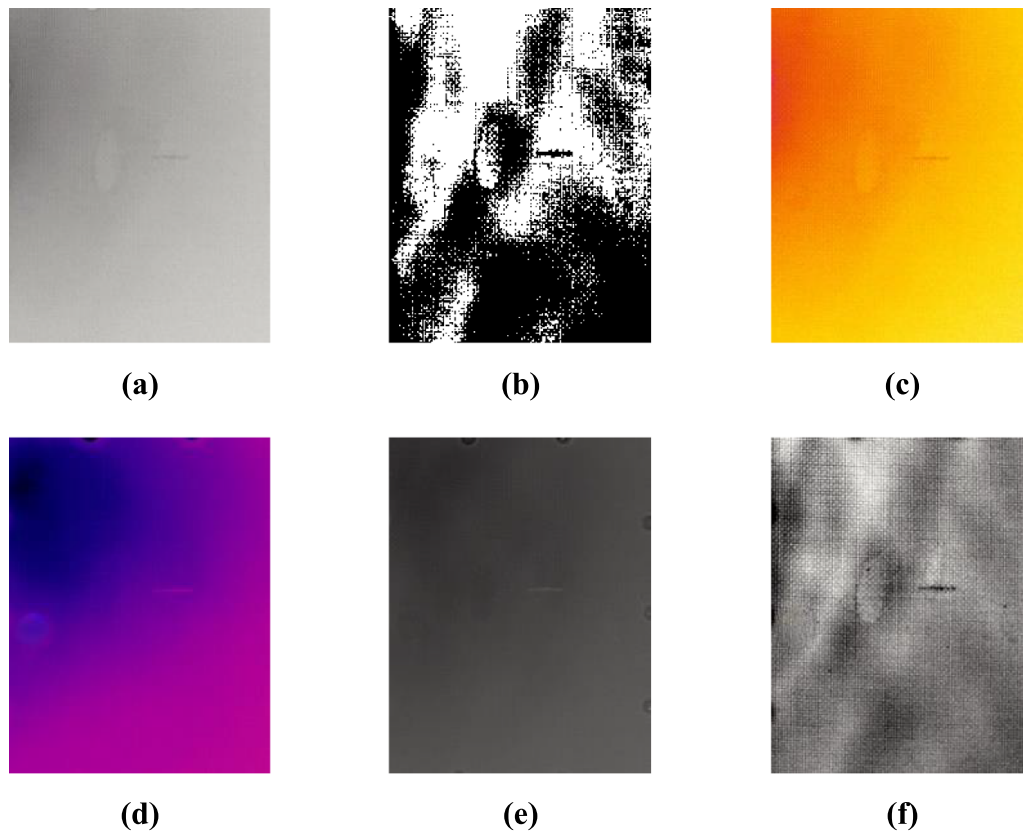$$AL = \bar{f} + PL \cdot \left(\max(f) - \bar{f}\right) \qquad (14)$$

Figure 17. Examples of maps for different parameters: (a–f) obtained for the sequence of thermograms.

Where: $\bar{f}$ is the MV of $f(i,j)$ for all measuring points and PL is the percentage level determined by the operator. All points, for which the $f(i,j) \geqslant$ AL should be carefully checked, as potentially damaged. The number or location of points satisfying the above inequality for different measurements can be compared with the aim of damage growth process observation.

As it is well known, the most important feature of ANN is the ability to generalization [44]. The used 'satisfactorily trained artificial neural network' formulation considered three points of view: minimization of the objective function (MSE) taking into account the network stop criteria, possibly high generalization abilities, and rationalization of the number of neurons in the hidden layer, which affects the time-consuming nature of calculations. The selection of the best ANN architecture was made based on the author's experience and data shown in figure 18; any precise formula was not determined in this aim.

In the presented paper, the shallow ANN is applied with one hidden layer. ANN is trained according to the Levenberg-Marquardt algorithm [45]. The minimized performance function was MSE and the additional stop criterion in the learning process was worded as follows: maximum epochs: 1000; performance goal: 0; minimum gradient: 1×10^{-7}; maximum validation checks: 6; training function parameter: 0.001 (with its decrease ratio equals 0.1, increase ratio equals 10, and maximal value 1e10). As input data, the network uses the location of the point in the thermogram (x and y coordinate, expressed by the row and column number, where the pixel corresponding
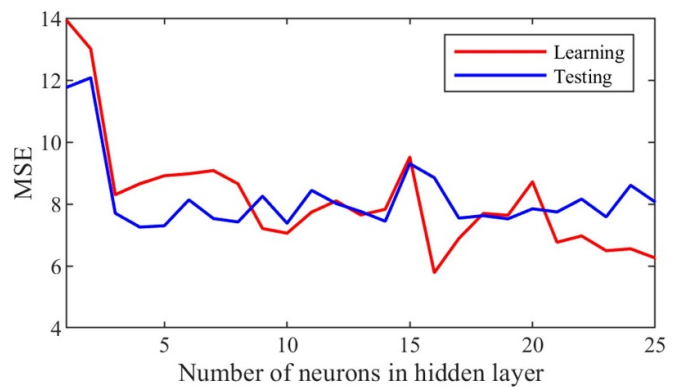

Figure 18. MSE (vs) number of neurons in the hidden layer.

to the measuring point are localized), and the output data are the value of the 2nd derivatives. So, the architecture of applied ANN is 2-H-1, where H is the number of neurons in the hidden layer. A varying number of hidden neurons is tested, and the best results are obtained for $H = 5$. The addition of hidden neurons did not significantly decrease the value MSE-figure 18, however, the usage of a more complicated model is also more time-consuming.

5.1.2. Damage verification using ANN-IRT results. In the presented case, the best results are obtained to analyze the second derivative of the thermal function (obtained from the
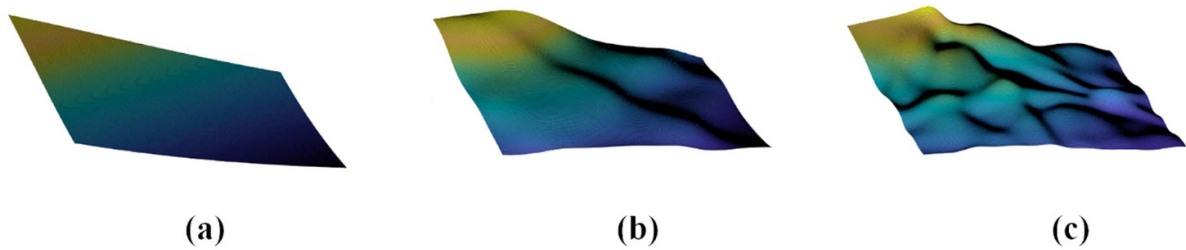
Figure 19. Surfaces approximated by ANN with the number of neurons in the hidden layer equals (a) 1, (b) 19, and (c) 30.
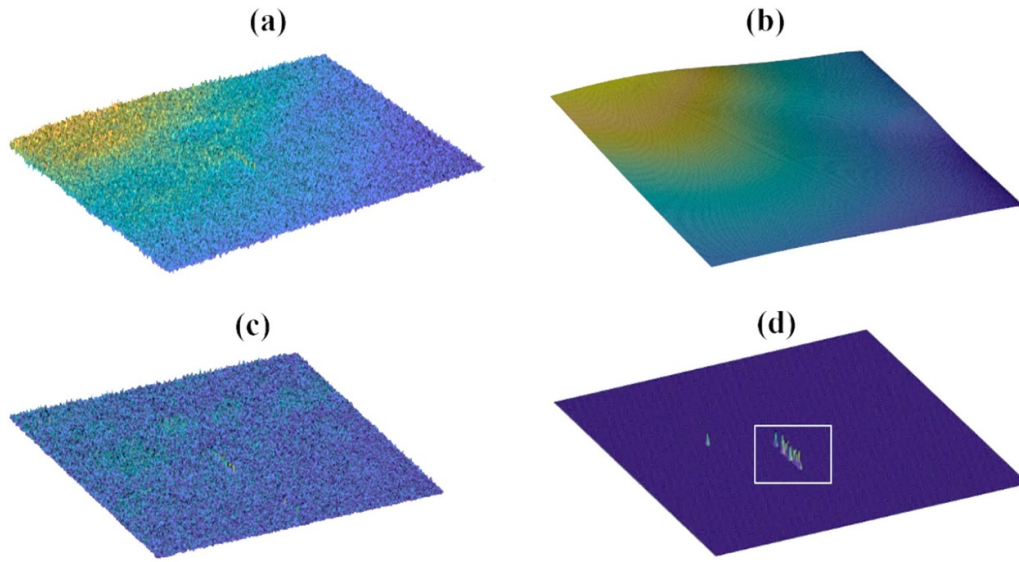

Figure 20. (a) Data imported from thermogram, (b) the second derivatives function distribution approximated by neural networks, (c) absolute value of the difference between (a) and (b), (d) the points showing the HLC damage considering the criterion given by the operator.

thermograms). In ANN-assisted IRT imaging, the main part of the control process can be made by machines. It can be assumed that suitable hardware for IRT imaging is mounted on the production line, which works continuously. Thanks to the suitable ANN-based software, the alarm is made only if some level of difference is exceeded. Then only this region can be controlled by specialists. The process is less time and cost-consuming.

From figure 17, even based on this function, the differences between HLC and the other regions are difficult to identify. The whole specimen is examined for precise indication of the damage, but further image analysis is made, omitting the regions where the PZT sensors are glued. ANN is one of the soft computing methods and is widely implemented in solving different problems like the prediction of material/component properties [37], optimization of the manufacturing process [46], as well anomaly [47], and damage detection [48]. The presented concept assumes the use of ANN for approximation of the 2nd derivatives distribution function. In figure 19, some examples of surfaces approximated by ANNs with different numbers of hidden neurons are shown.

The picture obtained from the IRT analysis is imported into the MATLAB environment. The colors of pixels on the picture correspond to the value of the analyzed parameters. Due to the greyscale, the values can vary at most from 0 to 255 for the whole thermogram as described previously in equation (10). The values for the region of interest are shown in figure 20(a). The difficulties in the differentiation of damaged regions are caused, e.g. by the heating process or structure of the material. During the experiment, the heat source is localized nearer to one side of the specimen than the others, so the points localized on this side have bigger temperature changes compared to the other points. It is visible on the diagram (figure 20(a)). This phenomenon generates the problem of determining the level of an analyzed parameter, which should raise the alarm.

The 2nd derivatives distribution function approximated by the ANN is shown in figure 20(b). Then the absolute value from the differences measured and using ANN obtained distribution is calculated, which is shown in figure 20(c). This approach eliminated the problem of uneven heating, but it is not enough. The differences between points are observed, which can be conditioned by the material structure. However, the HLC has the highest values of the analyzed function. To eliminate irrelevant changes, the alarm level is established (in the analyzed case, it is equal to $\text{mean}\,(\text{f}) + 40\%\,\{\max\,(\text{f}) - \text{mean}\,(\text{f})\}$); where f is the function presented in figure 20(c)-equation (11) with user inputs.
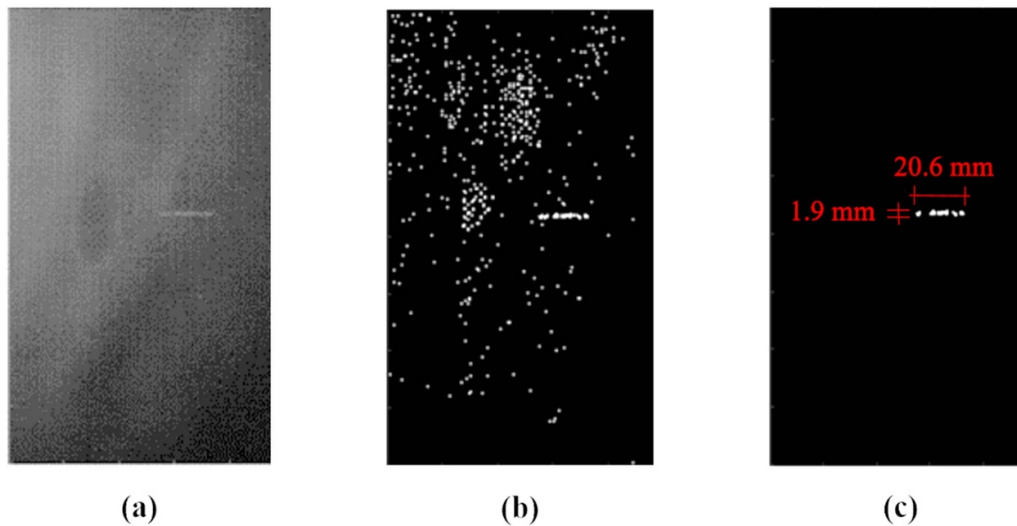
Figure 21. Case 2: (a) the second derivatives distribution image, (b) representation of pixels above alarm level, (c) thermogram after elimination of insignificant disorders (here, the maximal size of insignificant disorders is 2×2 px).
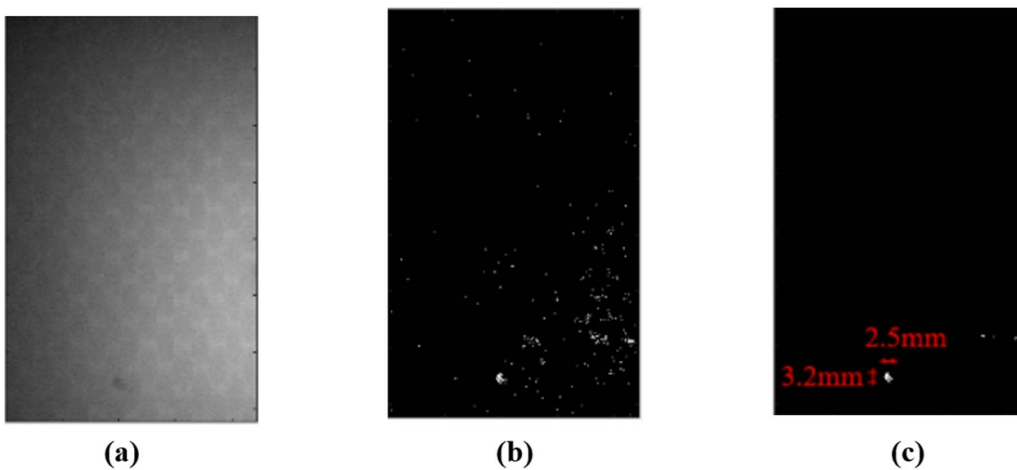

Figure 22. Case 1: (a) the second derivatives distribution image, (b) representation of pixels above alarm level, (c) thermogram after elimination of insignificant disorders (here, the maximal size of insignificant disorders is 2×2 px).

The AL has to be determined during the preparation of the tool and its adjustment to the examined material. It is necessary to observe the exemplary, well-known damage to differentiate it from normal changes caused by thermal distribution in heterogeneous materials. After the determination of the AL, it stays constant in further tests (e.g. with the aim of observation of damage growth). The values above the alarm level should be carefully examined. Some of them are only separated points (compare figures 21(b) and 22(b)) and should be omitted because they do not have the features of the crack, which are represented by a set of pixels adjacent to each other. The operator determines the size of areas for automatic deletion (here, all areas consisting of one or two adjacent pixels above alarm level, but surrounded by pixels below alarm level, are deleted; the result is shown in figures 20(d), 21(c) and 22(c)).

The main problem in automatic detection is differentiating the damage and the material with proper structure. Using grid

averaging may decrease the difference, and from the literature and known fact considering single points cannot be the damage, so they can be eliminated. The applied grid of points is the result of the resolution determined during the examination with IRT. The contrast between damaged and healthy zones could probably be bigger if the observed area is smaller (assuming constant resolution). However, it also means the necessity of more measurements for the same material area.

In figure 21, the consecutive steps in data processing are presented, showing the results after an application operator's determined parameters; from the 2nd derivative function (figure 21(a)) through the points considered potentially damaged (difference in values above the alarm level, shown in white color, figure 21(b) and finally after elimination of the points, which do not have the features of the cracks (figure 21(c)). A similar ANN process is also followed for Case 1 to obtain the results, as shown in figure 22. The approximate size of the damage is calculated by knowing the original

Table 7. Approximate damage dimensions obtained from IRT-ANN calculations.

Case	ADP (px)	ADD (mm^2)	Add (mm^2)	AD (mm^2)
1	7×9	Ø 11	Ø 5	Ø 6
2 -Subcase 3	43×4	20×10	20.6×1.9	0.6×0.9

size of the damage in pixels and comparing it against the approximated values of pixels from the predicted damage, as shown in figures 21(c) and 22(c). The approximate pixel matrix dimensions (Δx, Δy) obtained are 0.35 mm for case 1 and 0.48 mm for case 2 subcase 3. In table 7, the approximate dimensions of the estimated damages are presented and compared against the actual dimensions.

For case 1, the area of the counted significant pixels is 26 px $\times$ 0.35 mm $\times$ 0.35 mm = 3.18 mm^2 $\cong$ 3.2 mm^2. The shape of case 1 damage from the IRT image seems to be an irregular circle (figure 22(c)). In this scenario of the irregular circle, the area of the damage (D_c) is calculated using equation (15).

$$D_c = \pi \times \frac{D^2}{4} = \pi \times \frac{2.5 \text{ mm}^2}{4} = 4.9 \text{ mm}^2 \cong 5 \text{ mm}^2 \quad (15)$$

If a rectangular area is bound around the damage, the D_c value is 8 mm^2 (2.5 mm $\times$ 3.2 mm). The accuracy in damage size estimation of case 1 is relatively much lower than case 2-subcase 3 because IRT mainly picked the impact hit zone depth than the outer perimeter zone.

6. Conclusion

The following main findings are drawn from the analysis of the results.

- The SHM strategy based on the improved WTC algorithm is applied to the proposed MAE patch region, which effectively predicted the BVID region in case 1, and HLCs in case 2. The WTC algorithm effectively localized the damage with a few sensors.
- The newly implemented pixel counting-based confusion matrix method is applied to get an approximate size of the BVID and the length of HLC. The quantification results identified the damage with an error difference as low as 0.1 cm.
- A robust filtering method is required to locate the damage from the recorded thermograms as a heat source creates high thermal energy. ANN-IRT imaging algorithm is presented to differentiate the damaged shape from a high heat source. The developed ANN analysis with hidden neurons $H = 5$ model gave better results with reduced computational time. The ANN-IRT imaging algorithm quantified the approximate damage as close to an error difference as low as 0.6 cm.
- Overall, a robust SHM-NDT technique is implemented to study the different damage scenarios and obtain their characteristic shape and length, respectively.

Such global-local methods can be used in testing larger system-level components wherein SHM with sensors can localize the damages and NDT methods like IRT can be used to get more details about the damages. Further planned research involves implementing similar techniques in identifying hidden debonding and temperature-bound studies in composite structures.

Data availability statement

All data that support the findings of this study are included within the article (and any supplementary files).

ORCID iDs

Kaleeswaran Balasubramaniam https://orcid.org/0000-0001-9440-6068
Shirsendu Sikdar https://orcid.org/0000-0001-6897-0247
Dominika Ziaja https://orcid.org/0000-0002-8016-5504
Michał Jurek https://orcid.org/0000-0003-2645-7220
Rohan Soman https://orcid.org/0000-0002-5499-2565
Paweł Malinowski https://orcid.org/0000-0003-0478-2081

References

[1] Giurgiutiu V 2008 *Structural Health Monitoring* (London: Academic)
[2] Banerjee S, Ricci F, Shih F and Mal A 2007 Health monitoring of composite structures using ultrasonic guided waves *Advanced Ultrasonic Methods for Material and Structure Inspection* (Hoboken, NJ: John Wiley & Sons) pp 43–88
[3] Sohn H, Farrar C R, Hemez F M, Shunk D D, Stinemates D W, Nadler B R and Czarnecki J J 2003 *A Review of Structural Health Monitoring Literature: 1996–2001* (New Mexico: Los Alamos National Laboratory) p 1
[4] Peiponen K E, Zeitler A and Kuwata-Gonokami M (eds) 2012 *Terahertz Spectroscopy and Imaging* vol 171 (Berlin: Springer)

[5] Balasubramaniam K, Ziaja D, Jurek M, Fiborek P and Malinowski P 2021 Experimental and numerical analysis of multiple low-velocity impact damages in a glass fibered composite structure *Materials* **14** 7268

[6] Andreades C, Meo M and Ciampa F 2020 Tensile and fatigue testing of impacted smart CFRP composites with embedded PZT transducers for nonlinear ultrasonic monitoring of damage evolution *Smart Mater. Struct.* **29** 055034

[7] Su Z and Ye L 2009 *Identification Of Damage Using Lamb Waves* (Berlin: Springer)

[8] Moll J, Kexel C, Kathol J, Fritzen C, Moix-Bonet M, Willberg C, Rennoch M, Koerdt M and Herrmann A 2020 Guided waves for damage detection in complex composite structures: the influence of omega stringer and different reference damage size *Appl. Sci.* **10** 3068

[9] De Luca A, Caputo F, Sharif Khodaei Z and Aliabadi M 2018 Damage characterization of composite plates under low-velocity impact using ultrasonic guided waves *Composites* B **138** 168–80

[10] Spada A, Capriotti M and Di Scalea F L 2020 Global-Local model for guided wave scattering problems with application to defect characterization in built-up composite structures *Int. J. Solids Struct.* **182** 267–80

[11] Boettcher R, Kunik M, Eichmann S, Russell A and Mueller P 2017 Revisiting energy dissipation due to elastic waves at impact of spheres on large thick plates *Int. J. Impact Eng.* **104** 45–54

[12] Holst C, Lohweg V, Röckemann K and Steinmetz A 2019 Lamb wave-based quality inspection of repaired carbon fibre reinforced polymers for on-site aircraft maintenance *2019 24th IEEE Int. Conf. on Emerging Technologies and Factory Automation (ETFA)* (Zaragoza) pp 1643–6

[13] Lugovtsova Y, Bulling J, Mesnil O, Prager J, Gohlke D and Boller C 2021 Damage quantification in an aluminium-CFRP composite structure using guided wave wavenumber mapping: comparison of instantaneous and local wavenumber analyses *NDT&E Int.* **122** 102472

[14] Munian R, Roy Mahapatra D and Gopalakrishnan S 2020 Ultrasonic guided wave scattering due to delamination in curved composite structures *Compos. Struct.* **239** 111987

[15] Deng P, Saito O, Okabe Y and Soejima H 2020 Simplified modeling method of impact damage for numerical simulation of Lamb wave propagation in quasi-isotropic composite structures *Compos. Struct.* **243** 112150

[16] Segers J, Hedayatrasa S, Poelman G, Van Paepegem W and Kersemans M 2021 Nonlinear local wave-direction estimation for in-sight and out-of-sight damage localization in composite plates *NDT&E Int.* **119** 102412

[17] Sha G, Radzienski M, Soman R, Wandowski T, Cao M and Ostachowicz W 2020 Delamination imaging in laminated composite plates using 2D wavelet analysis of guided wavefields *Smart Mater. Struct.* **30** 015001

[18] Hervin F, Maio L and Fromme P 2021 Guided wave scattering at a delamination in a quasi-isotropic composite laminate: experiment and simulation *Compos. Struct.* **275** 114406

[19] Dafydd I and Sharif Khodaei Z 2019 Analysis of barely visible impact damage severity with ultrasonic guided Lamb waves *Struct. Health Monit.* **19** 1104–22

[20] Balasubramaniam K, Sikdar S, Soman R and Malinowski P 2022 Multi step structural health monitoring approaches in debonding assessment in a sandwich honeycomb composite structure using ultrasonic guided waves *Measurement* **194** 111057

[21] Azuara G and Barrera E 2020 Influence and compensation of temperature effects for damage detection and localization in aerospace composites *Sensors* **20** 4153

[22] Yue N, Khodaei Z and Aliabadi M 2021 Damage detection in large composite stiffened panels based on a novel SHM building block philosophy *Smart Mater. Struct.* **30** 045004

[23] Lambinet F and Khodaei Z 2020 Damage detection & localization on composite patch repair under different environmental effects *Eng. Res. Express* **2** 045032

[24] Malinowski P, Wandowski T and Ostachowicz W 2011 Damage detection potential of a triangular piezoelectric configuration *Mech. Syst. Signal Process.* **25** 2722–32

[25] Orłowska A, Kołakowski P and Holnicki-Szulc J 2011 Detecting delamination zones in composites by embedded electrical grid and thermographic methods *Smart Mater. Struct.* **20** 105009

[26] Poelman G, Hedayatrasa S, Segers J, Tellez J, Paepegem W and Kersemans M 2018 Optical infrared thermography of CFRP with artificial defects: performance of various post-processing techniques *Proceedings* **2** 457

[27] Meola C and Carlomagno G 2014 Infrared thermography to evaluate impact damage in glass/epoxy with manufacturing defects *Int. J. Impact Eng.* **67** 1–11

[28] Kappel S 2021 The Dispersion Calculator: a free software for calculating dispersion curves of guided waves in multilayered composites (available at: <www.dlr.de/zlp/en/ desktopdefault.aspx/tabid-14332/24874_read-61142/>) (Accessed 5 October 2022)

[29] Ostachowicz W, Soman R and Malinowski P 2019 Optimization of sensor placement for structural health monitoring: a review *Struct. Health Monit.* **18** 963–88

[30] Soman R, Kudela P and Malinowski P 2019 March. Improved damage isolation using guided waves based on optimized sensor placement *Sensors and Smart Structures Technologies for Civil, Mechanical, and Aerospace Systems 2019* vol 10970 (Denver, CO: SPIE) pp 51–64

[31] Ismail Z, Mustapha S, Fakih M A and Tarhini H 2020 Sensor placement optimization on complex and large metallic and composite structures *Struct. Health Monit.* **19** 262–80

[32] Angeloni G 2021 Carbon fiber, composite materials—G. Angeloni (available at: <www.g-angeloni.com//>) (Accessed 14 August 2022)

[33] Soman R 2022 Multi-objective optimization for joint actuator and sensor placement for guided waves based structural health monitoring using fibre Bragg grating sensors *Ultrasonics* **119** 106605

[34] Ceramtec.com 2021 CeramTec—The ceramic experts (available at: <www.ceramtec.com//>) (Accessed 10 July 2022)

[35] Rautela M and Gopalakrishnan S 2021 Ultrasonic guided wave based structural damage detection and localization using model assisted convolutional and recurrent neural networks *Expert Syst. Appl.* **167** 114189

[36] Sikdar S, Kundu A, Jurek M and Ostachowicz W 2019 Nondestructive analysis of debonds in a composite structure under variable temperature conditions *Sensors* **19** 3454

[37] Moustakidis S, Kappatos V, Karlsson P, Selcuk C, Gan T H and Hrissagis K 2014 An intelligent methodology for railways monitoring using ultrasonic guided waves *J. Nondestruct. Eval.* **33** 694–710

[38] Flir.eu 2021 Thermal Imaging, Night Vision and Infrared Camera Systems *Teledyne FLIR* (available at: <www.flir. eu/>) (Accessed 25 February 2022)

[39] AT—Automation Technology 2022 AT—Automation Technology: 3D Sensoren, Smart-Infrarotkameras, ZfP-Systeme und Thermografie-Lösungen zur Überwachung und Automatisierung (available at: <www. automationtechnology.de/>) (Accessed 4 June 2022)

[40] He Y, Gao B, Sophian A and Yang R 2017 *Transient Electromagnetic-thermal Nondestructive Testing: Pulsed Eddy Current and Transient Eddy Current Thermography* (Oxford: Butterworth-Heinemann)

[41] Sbarufatti C, Manson G and Worden K 2014 A numerically-enhanced machine learning approach to

damage diagnosis using a Lamb wave sensing network *J. Sound Vib.* **333** 4499–525

[42] Mahajan H and Banerjee S 2022 A machine learning framework for guided wave-based damage detection of rail head using surface-bonded piezoelectric wafer transducers *Mach. Learn. Appl.* **7** 100216

[43] Balasubramaniam K, Fiborek P, Ziaja D, Jurek M, Sawczak M, Soman R and Malinowski P H 2022 Global and local area inspection methods in damage detection of carbon fiber composite structures *Measurement* **187** 110336

[44] Lawrence S and Giles C L 2000 Overfitting and neural networks: conjugate gradient and backpropagation *Proc. of the IEEE-INNS-ENNS Int. Joint Conf. on Neural Networks. IJCNN 2000. Neural Computing: New Challenges and Perspectives for the New Millennium* (IEEE) vol 1 pp 114–9

[45] Sciencedirect.com 2021 Artificial intelligence in data mining *Science Direct* (available at: <www.sciencedirect.com/book/9780128206010/artificialintelligence-in-data-mining>) (Accessed 22 June 2022)

[46] Li Y, Lee T H, Wang C, Wang K, Tan C, Banu M and Hu S J 2018 An artificial neural network model for predicting joint performance in ultrasonic welding of composites *Proc. CIRP* **76** 85–88

[47] Ziaja D and Nazarko P 2021 SHM system for anomaly detection of bolted joints in engineering structures *Structures* **33** 3877–84

[48] Sikdar S, Liu D and Kundu A 2022 Acoustic emission data based deep learning approach for classification and detection of damage-sources in a composite panel *Composites* B **228** 109450